The Universality of Dark Matter Density Profiles for Milky Way Analog Galaxies

MARIA CLARA CAVALCANTE-SIVIERO , K. MENÉNDEZ-DELMESTRE , P. P. B. BEAKLINI , T. S. GONÇALVES , T. S. GONÇALVES , T. S. GONÇALVES , ARAUJO-CARVALHO , ARAUJO-CARVALHO , T. S. GONÇALVES , ARAUJO-CARVALHO , T. S. GONÇALVES , T. S. GONÇALVES , ARAUJO-CARVALHO , T. S. GONÇALVES , T. S. G

¹Brazilian Center for Research in Physics

² Federal University of Rio de Janeiro, Ladeira de Pedro Antônio 43, Rio de Janeiro, RJ 20080090, Brazil
 ³ National Radio Astronomy Observatory, Array Operations Center, Socorro, NM 87801, USA
 ⁴ Physics departament, Federal University of Espírito Santo, Vitória, ES, Brazil
 ⁵ European Southern Observatory, Garching, Germany

(Received October 30, 2025)

Submitted to ApJ

ABSTRACT

The structure, extent, and mass of the Milky Way's (MW) dark matter (DM) halo are observationally challenging to determine due to our position within the Galaxy. To overcome this limitation, we study a combined sample of 127 MW analogs from the IllustrisTNG-50 cosmological simulation with observations of 11 nearby galaxies. Using both spatial and spectral high-resolution data from VLA and GMRT telescopes, we employ the 3D-Barolo algorithm to derive precise kinematic maps and rotation curves (RCs). To perform a careful analysis of the stellar component, we use Spitzer mid-IR imaging at 3.6 and 4.5 μm . We decompose the RCs into their different mass components, enabling the construction of a DM radial profile for each galaxy. By using a MCMC-based routine, we account for the DM contribution for the observed RCs. For our simulated sample, we obtain DM radial profiles directly from the TNG50 database. We probe for the universality of the DM profiles by deriving and comparing the equivalent local DM density (LDMD), a critical parameter linked to DM direct detection experiments on Earth. We calculate the DM density at the corresponding location of the Sun in each of the analogs. Our analysis yields a final LDMD range of $0.17 - 0.46 \ GeV \ cm^{-3}$. Finally, by leveraging our mass estimates (M_{200} , M_{gas} and M_{\star}), we contextualize our findings with the efficiency of star formation in MW analogs and with the diversity of galaxies inhabiting similar halo masses.

1. INTRODUCTION

According to the Λ CDM cosmological model, baryonic matter constitutes only $\sim 15\%$ of the total matter content in the universe (Aghanim et al. 2020), with the remaining 85% attributed to the unseen component known as dark matter (DM). Despite many astrophysical evidences for the existence of DM, from galaxy rotation curves (RCs; Rubin et al. 1980; Bosma 1981; Sofue & Rubin 2001; Mancera Piña et al. 2022; Di Teodoro et al. 2022) to the large scale structure of the Universe (Davis et al. 1985; Navarro et al. 1996), the nature of DM still eludes us. The leading theoretical candidates are Weakly Interactive Massive Particles (WIMPs, Steigman & Turner 1985). These particles naturally arise in various extensions of the Standard Model of

Email: mariaclara@cbpf.br
* Valongo Observatory

particle physics and, within the Λ CDM paradigm, successfully satisfy cosmological constraints from the early universe. Specifically, cold DM (non relativistic at all times) is required to correctly form the observed cosmic structure (e.g. Riess et al. 1998; Spergel et al. 2007), as warmer, lighter particles would suppress the formation of small-scale halos where galaxies are formed (Tremaine & Gunn 1979; White et al. 1983). In agreement with the early suggestion by Peebles (1982) on the nature of cold DM, we assume that it might consist of a new, weakly interacting, neutral particle. Direct detection experiments on Earth aim to capture any phenomenological effect from DM particles interacting with standard matter. These experiments search for faint signals, such as phonons (heat), scintillations (light), or ionization (charge), generated by a hypothetical collision (recoil) between a DM particle and a target nucleus (see Undagoitia & Rauch 2015, for a extended review). The expected interaction rate for any given DM model is directly proportional to the DM density at a specific galactic address. Consequently, precise estimates of the local DM density (LDMD) are crucial for interpreting the results and setting constraints on particle physics parameters in experiments like those conducted by the XENON (Aprile et al. 2017) and LUX-ZEPLIN (LZ; Collaboration et al. 2015; Aalbers et al. 2023; Akerib et al. 2020) collaborations.

Historically, two primary approaches have been employed to estimate the LDMD in the MW. The first one relies on global mass modeling of the Galactic RC (e.g., Weber & de Boer 2010; Catena & Ullio 2010; Iocco et al. 2011; Sofue 2013, 2015). This method constructs mass models for the baryonic components (e.g., Salucci et al. 2010; Catena & Ullio 2010; Nesti & Salucci 2013; McMillan 2017; de Isídio et al. 2024) and fits a DM halo profile based on overall kinematics. While these models are often well motivated and can achieve uncertainties below $\sim 10\%$ (Catena & Ullio 2010; Iocco et al. 2015), they are fundamentally limited by their dependence on specific, and often debatable, assumptions regarding the shape of the DM halo (e.g., spherical versus triaxial; Reid et al. 2014; Palau & Miralda-Escudé 2023) and the mass-to-light ratios (M/L) of the baryonic components. The second approach makes use of local kinematic measurements from (mostly) stellar tracers (Kapteyn 1922; Oort 1932; Bovy & Tremaine 2012; Bienaymé, O. et al. 2014; Zhang et al. 2013). By inferring the gravitational potential from vertical motions of stars above the Galactic midplane, one can directly determine the LDMD without assuming a global halo model. However, this method presents its own challenges: many studies have found results consistent with $\rho_{DM} \approx 0$ even at the 3σ level, unless strong assumptions are made about the dynamics of the tracer population (Iocco et al. 2015). More recently, a third approach has been put forward to directly measure LDMD through stellar accelerations within the MW (e.g., Silverwood & Easther 2019; Chakrabarti et al. 2020). Direct measurement of these accelerations is achievable through high-precision techniques such as pulsar timing and the study of eclipsing binary stars (Chakrabarti et al. 2021; Chakrabarti et al. 2022). These approaches are particularly promising for probing DM sub-structure and will be complemented by next-generation time-domain facilities like the James Webb Space Telescope and Roman Space Telescope.

Recent work by de Isídio et al. (2024) points to the interest of studying external MW analogs to provide independent estimates of the LDMD. If DM is a universal component, its properties should be consistent across dynamically similar galactic environments. To date,

only a handful of nearby galaxies have been analyzed for this purpose, with de Isídio et al. (2024) presenting a sample of just five systems. They introduce a proof-ofconcept methodology, probing that baryonic mass modeling and RC decomposition approach can yield reliable estimates of the LDMD in MW-like galaxies. Despite the limited sample size, de Isídio et al. (2024) has successfully established external galaxies as valid laboratories for inferring the DM distribution of the MW itself. However, the lack of substantial statistics underscores the need for larger, more comprehensive samples. From a simulation perspective, a recent analysis by Pillepich et al. (2024) demonstrates that selecting MW analogs from the IllustrisTNG-50 cosmological simulation can effectively complement observational studies. These simulations provide access to a diverse population of galactic environments hosted by DM halos of similar mass, enabling systematic investigations of galaxy properties.

In this paper, we explore the DM density profiles for a combined sample of observed and simulated MW-analog galaxies. We combine an increasing number of observed galaxies with simulated halos, as a means to expand the breadth of galaxy properties with DM halos similar to our own. These external systems may provide reliable estimates for the MW's LDMD, thereby contributing to the increasingly narrow parameter space targeted by terrestrial direct detection experiments. This work not only assesses the mass components across a much broader sample of MW-like galaxies, but explores the connection between galaxies and their halos, revealing an underlying universality of the DM density profiles.

The remainder of this paper is organized as follows. Section 2 presents the observational data, including both newly acquired radio interferometric and archival infrared imaging. In Section 3, we present the sample selection and data from the IllustrisTNG-50 cosmological simulation. The methodology for kinematic modeling is detailed in Section 4. Section 5 presents our results and discussion. Finally, we summarize our conclusions in Section 6. We adopt a Λ CDM cosmology of plane geometry with $H=67.74~[km~s^{-1}~Mpc^{-1}]$, $\Omega_{\Lambda,0}=0.6911,~\Omega_{m,0}=0.3089,~\Omega_{b,0}=0.0486,~\sigma_8=0.8159$ and $n_s=0.9667$ (Aghanim et al. 2020).

2. OBSERVED MW ANALOGS AND DATA

In this work, we make use of HI kinematic data and stellar mass maps to construct and decompose RCs. To ensure the deepest coverage of stellar mass content in our sample, we select MW analog galaxies from the Spitzer Survey of Stellar Structure in Galaxies (S⁴G; Sheth et al. 2010; Muñoz-Mateos et al. 2013; Querejeta

et al. 2015; Watkins, A. E. et al. 2022), the and most homogeneous imaging for the largest sample of nearby galaxies at 3.6 and 4.5 μm , down to and equivalent mass surface density of 1 M_{\odot} pc^2 . For the HI gas dynamics we performed observations with the Karl G. Jansky Very Large Array (VLA) and the Giant Metrewave Radio Telescope (GMRT). The kinematic analysis is based on a combination of these acquired interferometric radio data.

2.1. Observations

2.1.1. Sample selection

We aim to investigate the dynamics and mass distribution in MW-like galaxies. For this, we base our selection on kinematic and morphological criteria: adopting a circular velocity at the Solar circle of $229 \pm 0.2 \ km \ s^{-1}$ (Eilers et al. 2019) and a maximum HI velocity range of $200 - 250 \ km^{-1}$ for the MW (Reid & Dame 2016), we choose galaxies with maximum HI velocities between 150 and 280 $km s^{-1}$. This ensures that our sample comprises galaxies with halo masses comparable to that of the MW (e.g., Posti & Helmi 2019). Considering that the MW is classified as SBb/c with a Hubble T-type in the range of 2-3 (Hou & Han 2014), we select galaxies within the range 1.5-4.5, extending the classification of the MW to include a broader range of late-type spirals (see Figure 1). We further restrict our sample to include galaxies suitable for reliable RCs, with inclinations between 35° and 75° .

HI data for five of these systems were already presented in de Isídio et al. (2024), based on VIVA (Chung et al. 2009) and THINGS (Walter et al. 2008) surveys. We expand the sample and complement their analysis with new VLA and GMRT HI observations for six new MW analogs. This results in a final observed sample of 11 galaxies. Mid-infrared images from S⁴G are available for all selected galaxies.

2.1.2. VLA observations

We observed four MW analogs (see Table 1) using the VLA array in C configuration at L-band (1 – 2 GHz) during March 2024, totaling \sim 17.3 hours (Proposal ID: VLA/24A-421; PI: K. Menéndez-Delmestre). The largest angular scale in C configuration is 970 arcsec (16.6 arcmin) and sets an upper size limit for detectable extended emission in this interferometric setup. All targets in our sample satisfy this constraint, with D_{25} diameters \leq 14 arcmin. We achieved a spectral resolution ranging from 3 to 13 km s⁻¹, by binning the requested resolution of 6 km s⁻¹ in eight channels. The observations provided a spatial resolution of 15–25", using 27 antennas with a maximum baseline of 3 km.

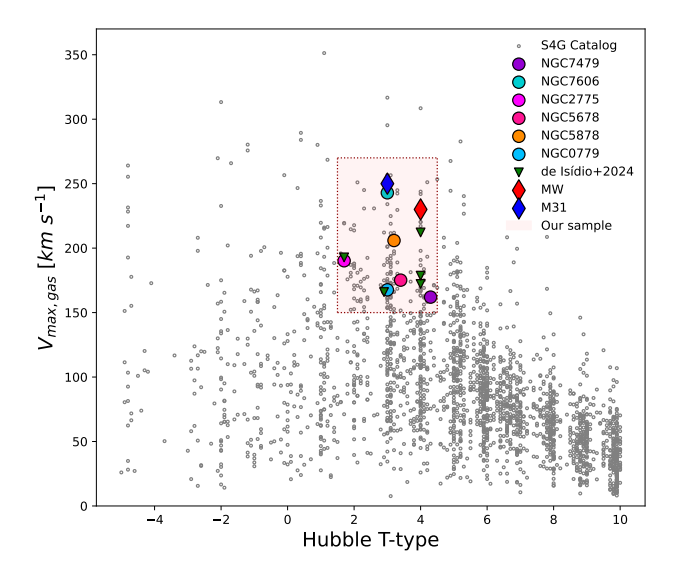


Figure 1. Sample selection from the S⁴G catalog. Gray points represent the full S⁴G sample. The light red shaded region indicates our selection criteria in the parameter space. Selected MW analog galaxies are highlighted with colored circles (this work) and green triangles (de Isídio et al. 2024). The Milky Way (MW; Reid & Dame 2016) and Andromeda (M31; Carignan et al. 2006) are shown for comparison as red and blue diamonds, respectively.

We performed data reduction and calibration using the COMMON ASTRONOMY SOFTWARE APPLICATIONS package (CASA Team et al. 2022, version 6.6.6). The VLA pipeline in CASA was used to apply standard bandpass, phase, and complex gain calibrations to the data. We also conducted continuum subtraction using line-free channels from the beginning and end of the observed cubes to isolate the HI line emission. We performed self-calibration for each VLA scheduling block using field sources to improve the signal-to-noise ratio in the final data cubes.

The achieved RMS noise levels are $5.7 \cdot 10^{-4} \, \mathrm{Jy} \, \mathrm{beam^{-1}}$ for NGC 7479 and $4.6 \cdot 10^{-4} \, \mathrm{Jy} \, \mathrm{beam^{-1}}$ for NGC 2775. Due to a shorter on-source integration time of only 2.7 hours, NGC 7606 exhibits a higher noise level of $1.4 \cdot 10^{-3} \, \mathrm{Jy} \, \mathrm{beam^{-1}}$. All data cubes were imaged using the TCLEAN task in CASA with WPROJECT gridder. We employed NATURAL weighting for NGC 7479 and NGC 2775, and BRIGGS weighting (robust=0.4) for NGC 7606. The deconvolution was performed with HOGBOM algorithm for NGC 7479 and MULTISCALE algorithm for NGC 7606 and NGC 2775. Figure 2 presents the resulting HI integrated intensity maps (moment 0) - generated by summing flux across all

channels with detected emission - and the corresponding line spectrum for each source.

2.1.3. GMRT observations

The observations with the GMRT telescope were conducted in April-July 2023 totaling ~ 40 hours (Proposal Code: 44.006; PI: K. Menéndez-Delmestre). This included 10 hours of on-source integration time per target for each of the four sources. Data were acquired in Band-5 (L-band; 1000–1450 MHz). Self-calibration procedure could not be applied to the GMRT observations due to the absence of suitable calibrator sources within the FOV of our target galaxies. The final data cubes reached a spatial resolution of 3-4 m and a spectral resolution of 3-4 km s⁻¹. Individual values for each galaxy are provided in Table 1.

In Figure 2 we also show the resulting HI integrated intensity maps and line spectra for the galaxies observed with the GMRT. These sources exhibit RMS noise levels of $8.3-8.8\cdot 10^{-4}$, approximately 20 times higher than those achieved on NGC 7479 and NGC 2775 with the VLA. For the GMRT data reduction, we used the TCLEAN task with WPROJECT gridder and MULTISCALE deconvolver for NGC 0779, and STANDARD gridder with HOGBOM algorithm for NGC 5678 and NGC 5878.

It is worth mentioning that the high spatial resolution achieved by mainly long baselines of the interferometer prevented the detection of large-scale, diffuse emission. This arises from a limited number of short baselines, which creates gaps in the uv-coverage that correspond to extended structures. Consequently, despite its superior spectral and spatial resolution, the GMRT data appear to recover only a fraction of the total HI flux, missing a significant portion of the large-scale, diffuse HI emission that dominates the outer disks (see Figure 2 for comparison with VLA observations). We therefore acknowledge that the derived HI mass estimates are likely lower limits.

3. MW ANALOGS FROM TNG50

We expand the sample of MW analogs in this work by including simulated MW analogs from the IllustrisTNG suite (The Next Generation; Pillepich et al. 2018; Nelson et al. 2019a) of cosmological hydrodynamical simulations. The IllustrisTNG represents a state-of-the-art framework for modeling universe evolution from redshift z=127 to z=0, featuring a comprehensive model of baryonic physics. These simulations incorporate stellar and AGN feedback, magnetic fields, and many sub-grid astrophysical processes, achieving unprecedented resolution. With sophisticated feedback prescriptions

and a 50 Mpc-on-a-side volume that affords high resolution (2160³ gas and DM cells, $m_{DM} = 8.5 \times 10^4$), IllustrisTNG-50 (hereafter TNG50; Pillepich et al. 2019; Nelson et al. 2019b) resolves galactic scales down to ~ 100 pc, enabling detailed comparisons between simulated and observed galaxy populations.

Similarly to our observational selection, we aim to select late-type galaxies similar to the MW, with similar DM halos. Considering the readily-available properties that the TNG50 database provides for all sub-halos, we based our selection on two main properties: the maximum rotation velocity (V_{max}) and the star formation rate (SFR). The maximum rotation velocity (V_{max}) , which includes the gravitational contribution of all particle types (gas, stars, DM, and black holes), allows for the selection of DM halos with total masses comparable to the MW's (Posti & Helmi 2019). We opted for the SFR criterium as a means to isolate late-type (disk) galaxies, which are characterized by active star formation. Based on these considerations, we select TNG50 subhalos at redshift z = 0 (Snapshot 99 in TNG50) requiring: (i) $1.0 < \text{SFR} < 8.5 \ M_{\odot} \ \text{yr}^{-1}$, consistent with MW values (Elia et al. 2022); and (ii) $200 < V_{\text{max}} < 315 \text{ km s}^{-1}$, based on the established range for the MW's circular velocity (Reid & Dame 2016) Applying these criteria resulted in a sample of 141 simulated MW-like systems. We further eliminate 14 systems with little or no DM particles $(M_{\star}/M_{DM} > 50 \%)$. We attribute these closeto-zero DM halos as potential results of galaxy mergers from which "chunks" of stellar mass were separated from their parent halos. These TNG50 subhalos, although they comply with our main selection criteria, appear to be environments in which all the DM was removed. We refer to these as systems with no cosmological origin, and we exclude them from our analysis. This result in a final sample of 127 simulated MW analogs from TNG50 suite.

4. ISOLATING THE DM COMPONENT IN OBSERVED AND SIMULATED MW ANALOG SAMPLES

The RC of a galaxy is a powerful dynamical tool for deriving its mass distribution, particularly for late-type systems (e.g. Sofue 2015). Decomposing the RC into its baryonic (stellar and gaseous) and DM components provides critical constraints on the properties of the DM halo, including its mass and radial extent (Di Cintio et al. 2013; Di Teodoro et al. 2022; de Isídio et al. 2024). In this work, we isolate the DM component in galaxies from both observational and simulation-based perspectives. The observational part involves the kinematic modeling of radio interferometric and mid-infrared data.

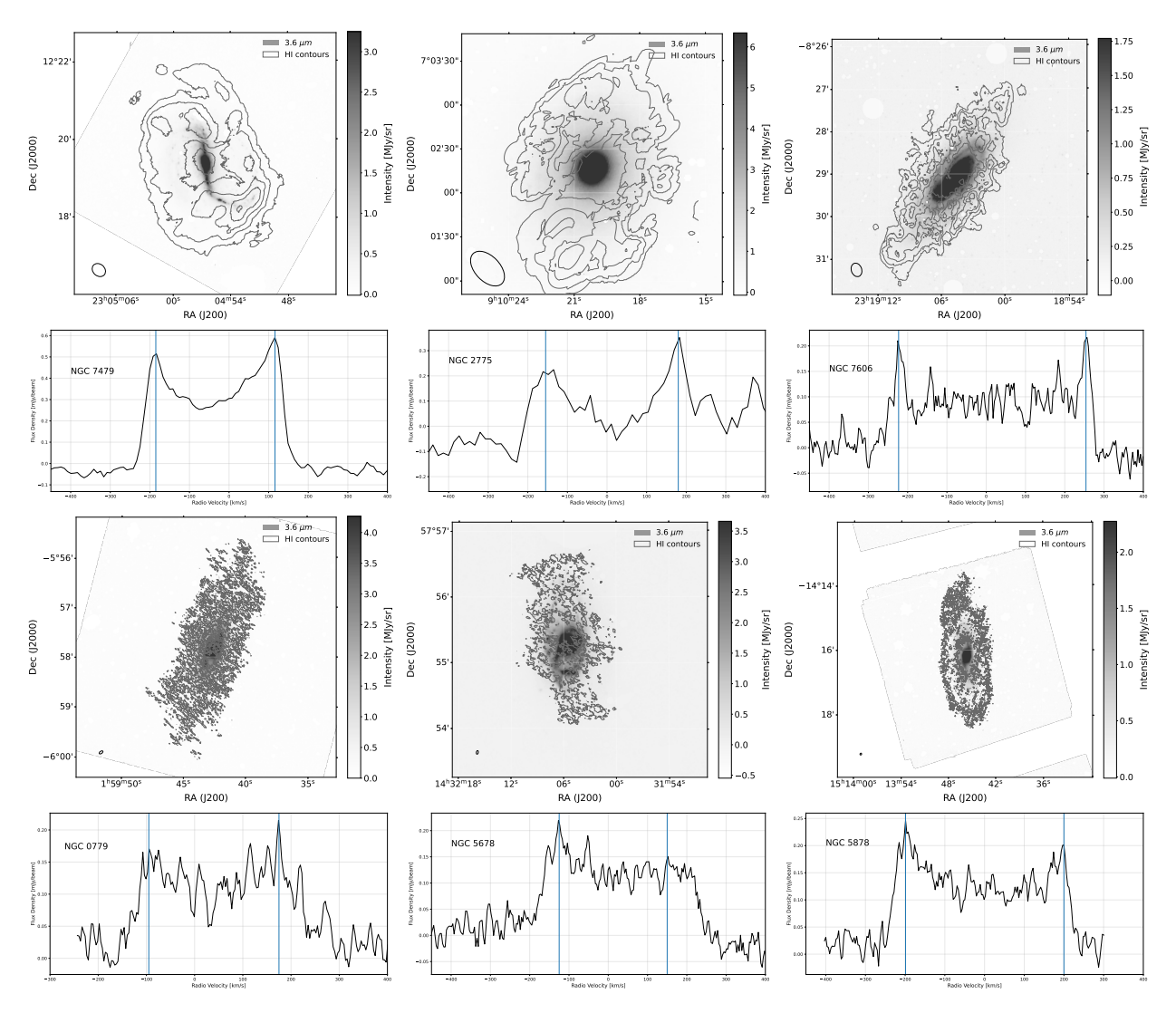


Figure 2. Rows 1 & 3: S⁴G mid-infrared images (Sheth et al. 2010) of our six MW analog galaxies with overlaid HI intensity contours, ordered by total observing time. The contours are based on the 0th moment map from 3D BAROLO (see Section 4.1 for details about the kinematic modeling). Contours are shown at 1, 2, 3, and 5σ levels for VLA sources, and at 2 and 5σ levels for GMRT sources. Rows 2 & 4: HI line spectra for the observed galaxies, corrected for optical redshifts. While the characteristic double-horn profile (indicated by the blue vertical lines) of a rotating disk is clearly detected in all galaxies, the GMRT data exhibit higher noise levels. See text for details.

In parallel, we analyze a wider sample of galaxies from the TNG50 cosmological simulation.

4.1. Rotation curve construction via kinematic modeling of HI data

Building RCs is an effective way of tracing the gravitational potential of spiral galaxies. These curves are typically derived through kinematic modeling, for which the tilted-ring model has provided an effective and widely used framework (e.g., Rogstad et al. 1974). This approach describes a galaxy as a series of concentric rings, each with its own kinematic properties. The main assumption is that the emitting gas is confined to a thin, rotating disk, and that the motion within each ring is

dominated by a constant circular velocity, dependent only on the galactocentric radius. Traditionally, tiltedring modeling was applied to two-dimensional (2D) velocity maps derived from observational data. However, a critical limitation of using 2D maps is their susceptibility to beam smearing, an effect that can severely bias the derived RCs, particularly in a galaxy's inner regions (Bosma 1978; Kamphuis et al. 2015; Biswas et al. 2023). To overcome these limitations, we employ the ^{3D}BAROLO software (Teodoro & Fraternali 2015), which constructs a fully 3D kinematic model of the galaxy directly from the HI data cube. This approach fits tilted rings in 3 dimensions, incorporating iterative corrections for inclination, position angle, and other parameters. By

Object	RA	DEC	Distance	Δt	Synt. beam	$\Delta \nu$	PA	Inc.	M_{HI}	M_{\star}	v_{HI}
	$[hh\ mm\ ss]$	$[dd\ mm\ ss]$	$[\mathrm{Mpc}]$	[hours]	$[arcsec^2]$	$[km\ s^{-1}]$	$[^o]$	$[^o]$	$[log_{10}($	$M/M_{\odot})]$	$[km\ s^{-1}]$
(1)	(2)	(3)	(4)	(5)	(6)	(7)	(8)	(9)	(10)	(11)	(12)
NGC7479	23 04 57.6	+12 19 48	33.39	6.9	20x3	9	207	43.00	9.91	11.02	240
NGC2775	$09\ 10\ 19.2$	$+07\ 02\ 24$	17.00	4.3	25x2	13	155	53.89	8.11	10.74	250
NGC7606	$23\ 19\ 04.8$	-08 28 48	31.55	2.7	15x1	3	145	66.76	9.68	10.84	270
NGC0779	$01\ 59\ 43.2$	-05 58 12	17.68	10	4x2	3	160	70.66	8.83	10.15	180
NGC5678	$14\ 32\ 04.8$	$+57\ 55\ 12$	29.47	10	3x0.5	3	183	63.53	9.51	10.72	200
NGC5878	$15\ 13\ 45.6$	-01 25 48	30.14	10	3x0.3	4	182	70.13	10.16	10.81	220

Table 1. Observational information and inferred properties for our sample of MW analog galaxies

NOTE—(1) Galaxy identifier; (2) Right ascension and (3) declination coordinates in J200 extracted from NASA/IPAC Extragalactic Database; (4) Galaxy distance extracted from NASA/IPAC Extragalactic Database; (5) Total time on source during our observations; (6) Major and minor synthesized beam axes; (7) Final velocity resolution in the HI data cubes; (8) Position angle and (9) Inclination inferred using the 3D Barolo algorithm; (10) Total HI mass calculated from the integrated HI flux using Equation 1 (Catinella et al. 2010); (11) Total stellar mass derived from 3.6 and 4.5 μ m fluxes using Equation 3 (Querejeta et al. 2015); (12) Maximum rotation velocity from the HI-derived RCs (see Figure 4).

explicitly accounting for instrumental effects during the model convolution step (see Teodoro & Fraternali 2015, for further details), 3D Barolo effectively mitigates biases from beam smearing and projection effects.

We performed an initial run to estimate the galaxy center coordinates, inclination, and position angle starting guesses. Input distances and initial guesses for maximum rotation velocities were adopted from the S^4G catalog (Sheth et al. 2010), while beam properties (major/minor axes, and position angle) were extracted directly from the HI imaging. The radial sampling (number of radii or radii separation between rings) was dynamically adjusted for each galaxy based on beam size, with multiple tests conducted to optimize the RC fit and minimize residuals. ^{3D}BAROLO uses a mask to identify the regions in the cube where galaxy emission is; to generate this mask we used the built-in Search mode algorithm. Figure 3 presents the derived kinematic maps: the line-of-sight velocity (1st moment) and velocity dispersion (2nd moment) for each observed galaxy. Both the receding and approaching sides of the galaxies were fitted. The resulting RCs (shown in Figure X) arise from averaging the final velocity values from both sides at equal radial distances from the center.

4.2. Mass decomposition

To robustly isolate the DM component, we account for baryonic mass distributions by directly measuring gas and stellar contributions.

4.2.1. Gas component

In spiral galaxies, HI typically constitutes $\sim 70-80\%$ of the total gas mass (Saintonge & Catinella 2022). To account for the contribution of Helium and heavier elements, we apply a correction factor of 1.36 to the derived

HI mass (Chowdhury et al. 2022). Given that molecular gas (H_2) is not a dominant mass component in the outer disks of spiral galaxies we omit its contribution from our mass model (see Mancera Piña et al. 2022 for H_2 and CO kinematic modeling). To calculate the HI masses we adopt the mass relation from Catinella et al. (2010):

$$M_{HI} = \frac{2.356 \times 10^5}{1+z} \left[\frac{d_L(z)}{Mpc} \right]^2 \left[\frac{S_{HI}}{Jy \ km \ s^{-1}} \right]$$
 (1)

where $d_L(z)$ is the luminosity distance at redshift z and S_{HI} is the integrated flux. The integrated flux is obtained by summing over all source-detected pixels and velocity channels in the data cube:

$$S_{HI} = \sum F_{HI} \Delta \nu \tag{2}$$

where F_{HI} is the HI flux measured in each channel and $\Delta\nu$ is the HI data cube bandwidth. The spatial distribution of this integrated flux is shown in the 0th moment maps presented in Figure 2. The derived HI masses for all observed sources in our sample are presented in Table 1.

The ^{3D}BAROLO algorithm calculates the surface mass density of the cold atomic gas directly from the data cube, enabling a direct derivation of the gravitational potential. This is achieved by summing the HI signal within concentric tilted rings and applying corrections for the galaxy's inclination and position angle.

4.2.2. Stellar component

Following the same methodology applied to the gas decomposition, we sum the mid-infrared flux within concentric annuli matching those derived by 3D Barolo for each HI data cube. This ensures consistent radial sampling when comparing gas and stellar distributions. For

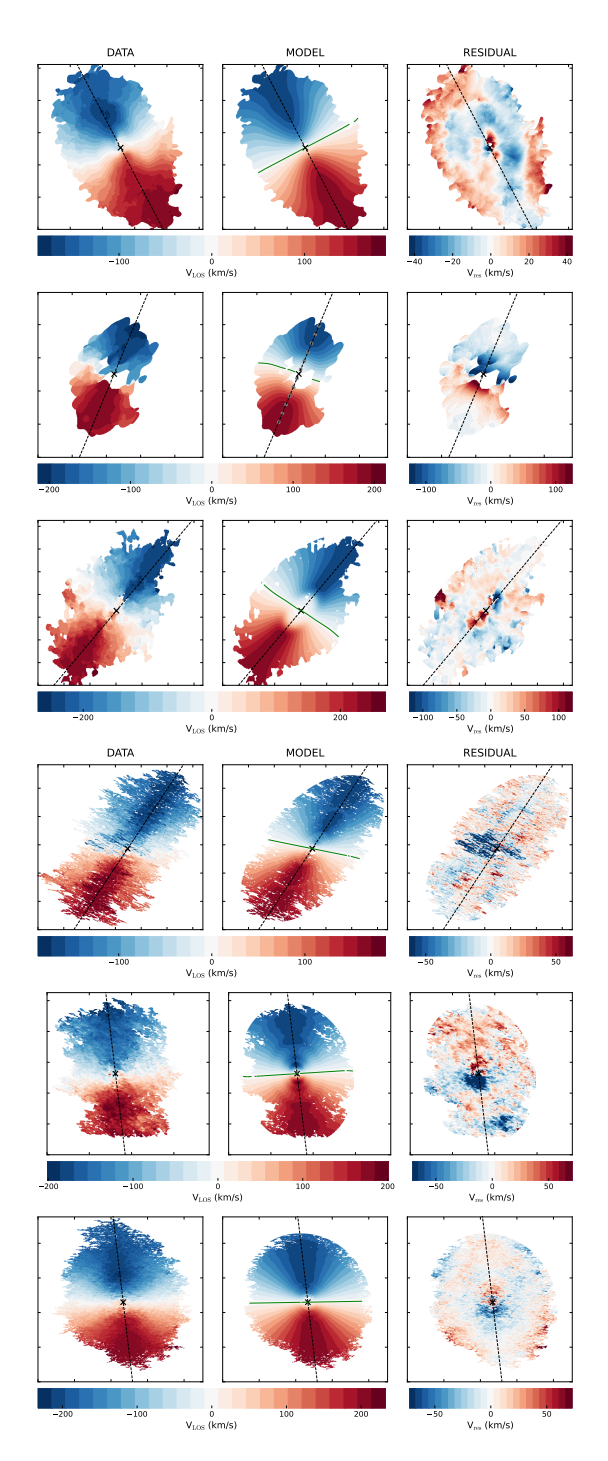


Figure 3. Velocity maps (1st moment) for the observed galaxies: (a) NGC 7479, (b) NGC 2775, (c) NGC 7606, (d) NGC 0779, (e) NGC 5678, and (f) NGC 5878. First column: HI velocity field derived from the radio data cubes. Second column: 2D projection of the 3D kinematic model generated by ^{3D}BAROLO. Third column: Residuals (data — model). The dashed black curve traces the kinematic major axis for each galaxy, as determined by the best-fit inclination and position angle parameters from the ^{3D}BAROLO modeling. The solid green line indicates where the kinematic transition occurs between the receding (redshifted) and approaching (blueshifted) sides.

the stellar mass conversion, we apply the empirical relation from Querejeta et al. (2015):

$$M_{\star} = 10^{8.35} \left[\frac{F_{3.6\mu m}}{Jy} \right]^{1.85} \left[\frac{F_{4.5\mu m}}{Jy} \right]^{-0.85} \left[\frac{D}{Mpc} \right]^{2}$$
 (3)

where $F_{3.6\mu m}$ and $F_{4.5\mu m}$ are the 3.6 and $4.5\mu m$ band fluxes and D is the galaxy distance. The derived stellar masses for all observed sources in our sample are presented in Table 1.

4.2.3. Dark matter halo profile

Although debates persist regarding a diversity of DM density profiles in late-type galaxies (e.g., Oman et al. 2015), the NFW profile remains one of the most widely supported models for reproducing the circular velocities of disc systems (Salucci et al. 2007; Di Cintio et al. 2013; Iocco et al. 2015; Pato & Iocco 2015). We assume an NFW profile and determine a set of virial mass (M_{200}) and concentration (c) parameters for each galaxy, following the methodology detailed in de Isídio et al. (2024), briefly described here.

Considering that the DM halo is gravitationally coupled with stellar and gaseous mass distributions, the inferred halo parameters directly depend on the baryonic kinematics. To estimate M_{200} and c for the RC of each galaxy in our sample, we perform a Markov Chain Monte Carlo (MCMC) analysis - implemented with the Python package emcee (Foreman-Mackey et al. 2013). For each galaxy, we use 50 walkers and run 30,000 iterations, discarding the first 25% of each chain as burn-in. In addition to this approach from de Isídio et al. (2024), we constrain the parameter space of M_{200} and c, by adopting the concentration-mass relation derived by Dutton & Macciò (2014):

$$\log_{10}(c) = 0.905 - 0.101 \log_{10} \left(\frac{M_{200}}{10^{12} \ h^{-1} \ M_{\odot}} \right). \tag{4}$$

We set flat priors for the halo mass over the range $9 < log(M_{200}/M_{\odot}) < 13$ and for the concentration parameter over 1 < c < 50. The resulting best-fit parameters and their uncertainties from our MCMC analysis are reported in Table 2.

4.3. Rotation curve decomposition

To derive the circular velocity contribution from each baryonic component, we calculate the gravitational potential generated by a razor-thin axisymmetric disk with a given surface mass density $\Sigma_{baryon(R)}$:

Table 2. Best-fit halo parameters and LDMD from the MCMC analysis

Object	$log_{10}(\frac{M_{200}}{M_{\odot}})^{+\sigma}_{-\sigma}$	$c^{+\sigma}_{-\sigma}$	$\frac{\rho_{DM}}{GeV\ cm^{-3}}$	χ^2/ν
(1)	(2)	(3)	(4)	(5)
NGC 7479	$12.12^{+0.11}_{-0.09}$	$8.82^{+1.45}_{-1.29}$	0.173	0.5173
NGC 2775	$12.21^{+0.35}_{-0.24}$	$24.58^{+7.49}_{-6.50}$	1.770	8.9909
NGC 7606	$12.30^{+0.11}_{-0.09}$	$17.62^{+3.13}_{-2.71}$	0.308	0.6678
NGC 0779	$11.64^{+0.15}_{-0.12}$	$24.39^{+5.12}_{-4.40}$	1.230	0.6880
NGC 5678	$11.90^{+0.21}_{-0.16}$	$17.43^{+4.17}_{-3.63}$	0.197	0.5387
NGC 5878	$11.47^{+0.04}_{-0.04}$	$26.24^{+3.57}_{-3.15}$	0.233	0.3638

Note—(1) Galaxy identifier; (2) Halo mass M_{200} and (3) concentration parameter c, showing their best-fits values with respective lower and upper errors from the MCMC analysis; (4) DM density at the solar equivalent position in each MW analog $(R_{\odot} = 1.8 \times R_{eff})$, see Section 5.1 for details); (5) Reduced χ^2 statistic.

$$\Phi_{baryon} = -4 G \int_0^{r_{max}} R' \Sigma_{baryon(R')} \frac{K\left(\frac{4RR'}{(R+R')^2}\right)}{|R+R'|} dR'$$
(5)

where G is the gravitational constant, $\Sigma_{\text{baryon}}(R')$ is the surface density at radius R', and K(m) is the complete elliptic integral of the first kind, defined as:

$$K(m) = \int_0^{\frac{\pi}{2}} \frac{d\theta}{\sqrt{1 - msen^2\theta}} \tag{6}$$

The total circular velocity model, $V_{mod(R)}$, is constructed from the quadratic sum of the individual contributions from the stellar, gaseous, and DM halo components:

$$V_{mod} = \sqrt{V_{\star}|V_{\star}| + V_{gas}|V_{gas}| + V_{DM}|V_{DM}|}$$
 (7)

The final RC decompositions for the six observed MW analog galaxies in this work are presented in Figure 4. For every system, the modeled circular velocity (based on the NFW DM halo contribution) closely reproduces the observed rotation curves, as evidenced by the small residuals. In most galaxies, the DM component already dominates the gravitational potential at the equivalent solar neighborhood position, whereas the stellar component is dominant in the innermost regions. The only exception is NGC 7479, where the stellar contribution exceeds that of the DM halo out to approximately 3 ef-

fective radii⁶ (R_{eff}) , after which the DM starts to dominate. The contribution from the gaseous disk is generally minor to the total mass budget, particularly in the central regions where its surface density approaches zero. The velocity profiles derived for gas typically exhibit a smooth rise and maintain a nearly constant value in the outer disks. NGC 5878 presents a unique case in which the gas component exceeds the stellar contribution at larger radii. This can be explained by its high concentration (c = 26.24) and lower halo mass $(11.47 \log(M_{halo}/M_{\odot}))$, as we will discuss in further detail in the next section. Despite the crucial role that extended gas plays in tracing the dynamics and total mass of galaxies, the DM halo and stellar disk remain the primary sources of gravitational potential at the equivalent Solar circle, in agreement with recent work (de Isídio et al. 2024).

4.4. Rotation curves and dark matter profiles in TNG50 MW analogs

The methodology for deriving kinematics and DM profiles from the TNG50 simulation is more straightforward, as it relies on direct access to the mass distribution of each particle type. This allows us to precisely calculate the gravitational potential and the dynamical contribution of each component (DM, stars, gas) at any point. Notwithstanding, we must still adopt two key assumptions to infer the circular velocity profile, $v_{\rm circ}(r)$: 1) the DM halos are assumed to exhibit approximate spherical symmetry and 2) the gravitational force is assumed to be balanced by the centrifugal force:

$$\frac{m\ V^2}{r} = \frac{G\ M\ m}{r^2} \ \therefore \ V_{circ}(r) = \sqrt{\frac{G\ M(r)}{r}}$$
 (8)

Based on these physically motivated conjectures, we perform a mass decomposition and RC analysis on the simulated sample, similar to the methodology applied to our observational data. For each system, we calculate the enclosed mass by summing all particle types within concentric spherical shells of 0.1 kpc width, extending from the galactic center to the outermost bound particle, a radius that can reach several hundred kpc for the most massive halos.

The circular velocity is then derived from the total enclosed mass, M(< r), using Eq. 8. For our final sample

 $^{^6}$ The effective radius $(R_{\rm eff})$ is defined as the semi-major axis length of the elliptical isophote that encloses half of the galaxy's total stellar light. We obtained effective radii for all S $^4{\rm G}$ galaxies (Muñoz-Mateus, private communication), based on Munoz-Mateos et al. 2015

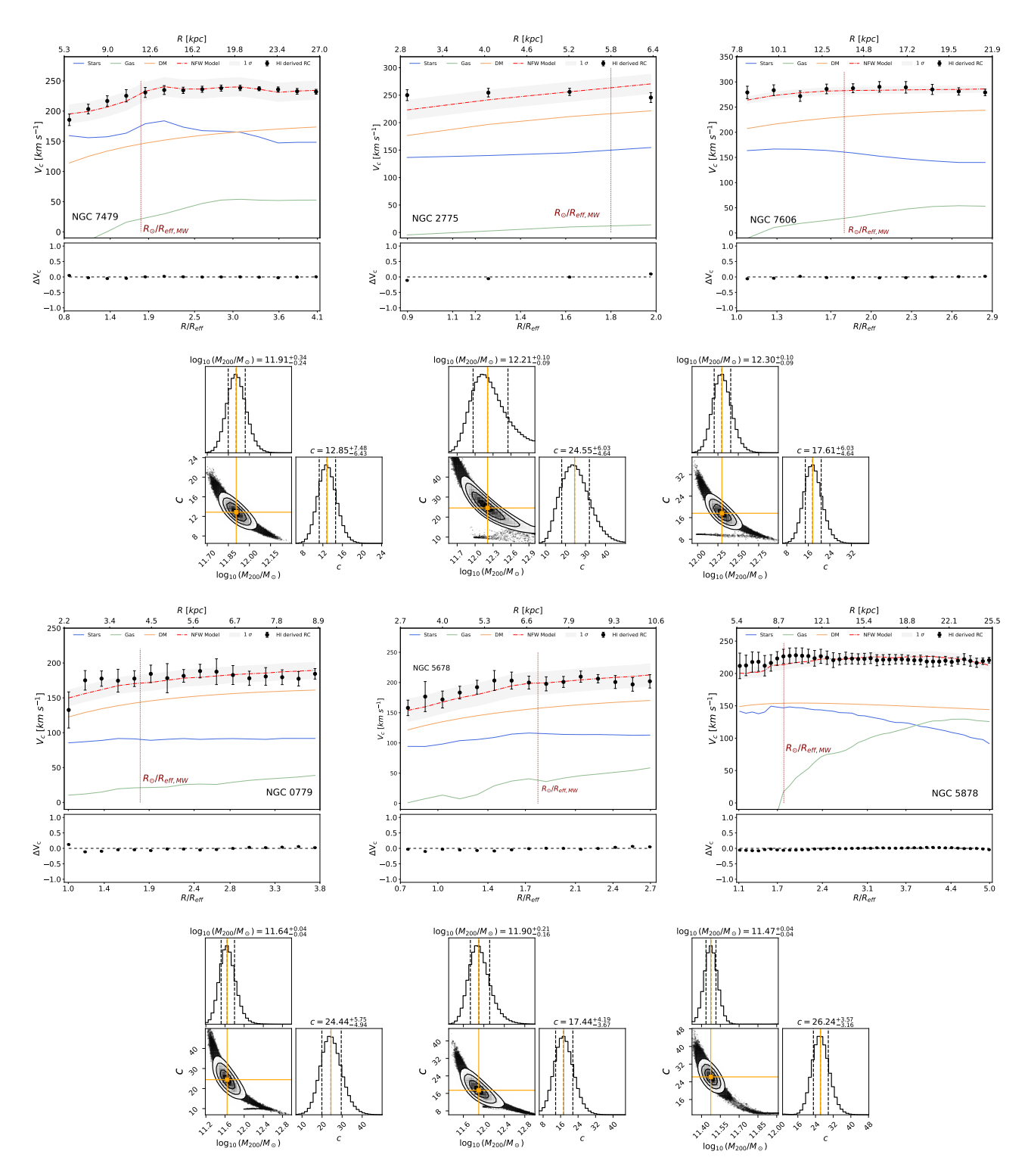


Figure 4. Rotation curve (RC) decomposition and best-fit NFW parameters for the observed galaxies. Rows 1 & 3: Decomposed RCs for (a) NGC 7479, (b) NGC 7606, (c) NGC 2775, (d) NGC 0779, (e) NGC 5678, and (f) NGC 5878. Each panel shows the HI-derived circular velocity (black points; $v_{\rm circ}$), the total best-fit model (red dash-dotted line; $v_{\rm mod}$), and contributions from gas (green), stars (blue), and the NFW halo (orange). The vertical dark red line marks the equivalent Solar neighborhood at $R = 1.8 \times R_{\rm eff}$ (Licquia & Newman 2015). The lower panel displays the normalized residuals $(v_{\rm mod} - v_{\rm obs})/v_{\rm obs}$. Rows 2 & 4: Posterior distributions for the best-fit NFW parameters (M_{200} , c) from our MCMC analysis, corresponding to the RCs directly above them. These results are essential for the stellar-to-halo mass (SHMR) and concentration-mass ($c - M_{200}$) relations discussed in Section 5.

of 127 MW-like galaxies, we generate RCs by quadratically summing the contributions from stars, gas, and DM. Figure 5 presents the resulting RCs for the full simulated sample, color-coded by stellar mass. For comparison, we include the high precision RC derived for the MW by Eilers et al. (2019). The RCs of the simulated galaxies reproduce the same features as the MW: a steep inner rise followed by a flat outer profile. The radius at which the RCs flatten exhibits significant scatter ($\sim 0.1 - 1 R_{eff}$), which is correlated with their halo concentration (Posti, Lorenzo et al. 2019b). We note that galaxies with lower stellar mass consistently reach their peak circular velocity at lower values. This is an expected trend (e.g., Posti & Fall 2021; Posti, Lorenzo et al. 2019b), considering that stellar mass is also an important tracer of the gravitational potential. However, we also identify lower stellar mass galaxies with higher flat rotation velocities. In these cases, a significant contribution from other mass components, such as an extended and massive gas disk can account for the elevated velocities. Consequently, by defining our sample of simulated MW analogs based on maximum rotation velocity, we effectively restrict the halo mass parameter space without imposing a direct limit on stellar mass. The range of colors in Figure 5 reflects this diversity, illustrating the variation in stellar mass that can reside within halos of $M_{200} \gtrsim 10^{12} M_{\odot}$.

We derive DM density profiles for the TNG50 galaxies in our sample, based on the the mass enclosed in successive spherical shells, without assuming any specific profile. These profiles are presented in Figure 6, alongside the inferred profiles of our observational sample, which comprises the six galaxies from this work (described in Section 4.2.3) combined with five systems from de Isídio et al. (2024).

5. RESULTS AND DISCUSSION

5.1. Local dark matter density

Measuring the DM at the Solar neighborhood is a very challenging task. This difficulty arises not only from our embedded position within the system, which introduces strong observational biases (Licquia & Newman 2015), but also from the numerous assumptions and approximations required to derive this quantity (Catena & Ullio 2010; Salucci et al. 2010; Reid et al. 2014). We use external galaxies with similar DM halos in an effort to draw analogies with our own. By deriving the DM density radial profiles in these MW analogs, we can estimate the typical dark-matter density range at the Solar-equivalent radius.

The DM density radial profiles that we derived for our sample of observed and simulated MW analogs are

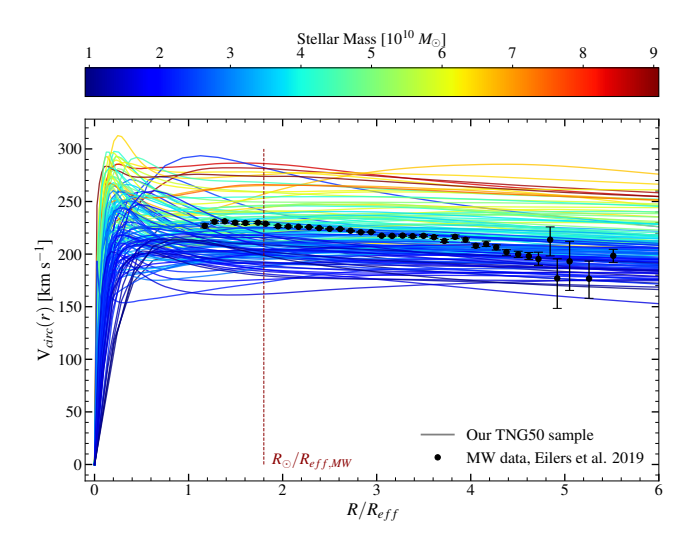


Figure 5. Rotation curves (RCs) for 127 Milky Way (MW) analogs systems from the Illustris TNG-50 cosmological simulation. Curves are color-coded by stellar mass, spanning a range of $1-9\times10^{10}~M_{\odot}$. We also add the derived RC for the MW in Eilers et al. (2019), in black data points. All radii are normalized by the stellar effective radius ($R_{\rm eff}$), taken directly from the simulation.

presented in Figure 6. To enable a direct comparison between our sample of analog galaxies and the MW, we parametrize galactocentric distances in terms of the galaxy's stellar effective radius (R_{eff}) . Adopting a disk scale length for the MW of 2.6 kpc, we obtain an effective radius of $R_{\rm eff,MW} = 4.5~{\rm kpc}$ (Licquia & Newman 2015; Zhou et al. 2023). The Solar radius can thus be expressed as $R_{\odot} \approx 1.8 \times R_{\rm eff,MW}$. With S4G effective radii available for our observed sample, we show in Figure 6 the DM radial density profiles of our sample in units of Reff, allowing for an immediate appreciation of the range in DM density values that our sample galaxies exhibit at the galactocentric distance that corresponds to the Sun's location in the MW. For the TNG50 sample of MW analogs, we do not have available effective radii attached to light distributions. However, considering that age, metallicity and extinction radial gradients have very little impact in the mid-IR emission (Munoz-Mateos et al. 2015), we use the half-mass radius provided by the TNG50 database as an equivalent radial parametrization to the one we use for our observed sample. We show the median LDMD derived from our TNG50 sample in Figure 6. This value shows excellent agreement with the range estimated for the MW in Iocco et al. (2011).

We note that the MW's bar, with semi-major axis of 4 kpc (corresponding to 0.9 Reff), points to a lack of spherical symmetry in these inner regions. However, the region of interest in this study is the radial posi-

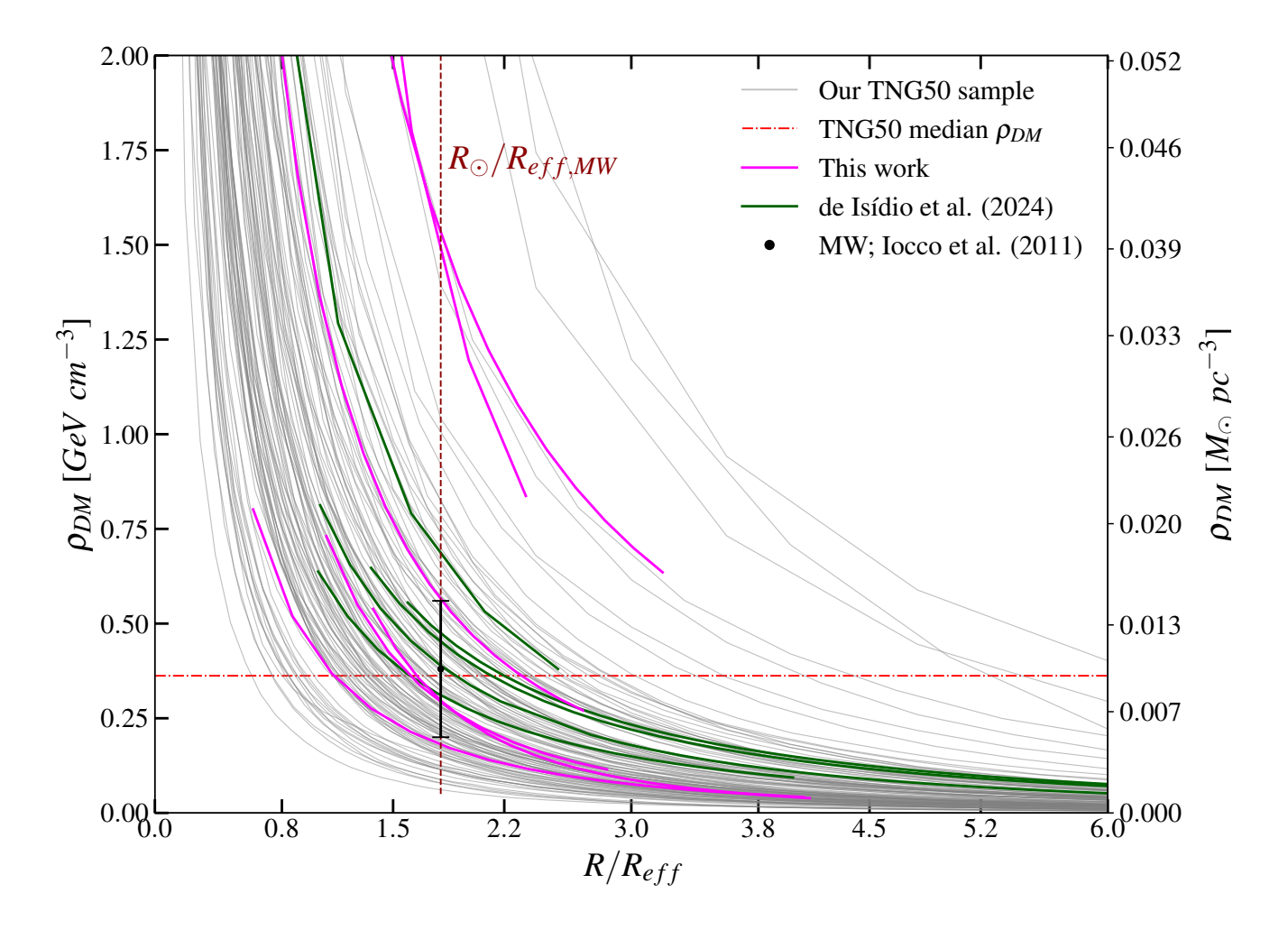


Figure 6. DM density profiles for our sample of 138 MW-like systems. Gray solid lines represent the radial DM density profiles for 127 simulated subhalos from the IllustrisTNG-50 cosmological simulation, calculated in concentric spherical shells of 0.1 kpc width. Colored solid curves show the DM density profiles derived from the best-fit NFW parameters of our MCMC analysis for the observational sample. The equivalent Solar neighborhood radius, defined as $1.8 \times R_{\rm eff}$, is indicated by the vertical dashed dark red line. The black interval denotes the range of LDMD for the MW from Iocco et al. (2011), based on microlensing and kinematic measurements. The red dash-dotted horizontal line marks the median LDMD ($\rho_{\rm DM}=0.39~{\rm GeV~cm^{-3}}$) derived from our TNG50 sample. For consistency with simulation-based studies (e.g., Pillepich et al. 2024), DM density is also shown in units of ${\rm M}_{\odot}~{\rm pc}^{-3}$ on a complementary axis.

tion of the Sun in the MW and the resulting DM profiles in our study cover the radial range between 1Reff and 2-5 Reff, thereby excluding potentially complex bardominated regions.

Figure 6 shows that the TNG50 simulated sample displays a broader range in DM density values at the equivalent Solar location, encompassing both higher and lower values than those seen in observations. We attribute this difference primarily to the size differences between the two samples: the observed sample, by the challenging nature of the observations, is quite limited,

whereas the TNG50 simulation provides a diverse population of over a hundred systems with matched mass, kinematics, and morphological properties. The DM density profiles derived in de Isídio et al. (2024) show good agreement with that of four galaxies observed in this work and are consistent with the overall distribution of profiles from our simulated galaxies.

Within the TNG50 sample, we identify 8 systems with particularly high DM content that nonetheless satisfy our selection criteria for MW-like galaxies. Although these systems could potentially be distinguished from

the rest based on their compactness or their low stellar mass (i.e., $(\log(M_{\star}/M_{\odot}) < 10)$, we note that their DM profiles share similarities with the 2 outliers from our observed sample. In total, these 10 systems (8 simulated, 2 observed) represent the most significant outliers in our analysis, characterized by their compact size, lower rotational support and, for the observed ones, their proximity ($\lesssim 17 \ Mpc$).

Figure 7 shows the distribution of the LDMD calculated at the equivalent Solar position within our simulated sample (127 subhalos), compared to that derived by Pillepich et al. (2024) for their MW analog sample (130 subhalos) using our definition of the solar position. Our selection criteria yield a narrower LDMD distribution, peaking within the range reported by most previous MW studies: 0.34 GeV cm⁻³ (equivalent to $\approx 0.009 \ M_{\odot} \ \mathrm{pc^{-3}}$; see Table 3 for a compilation of references). We also include data points derived from our observational analysis, vertically positioned according to their R_{eff} , with error bars estimated from our MCMC analysis. We find that systems with the smallest R_{eff} (NGC 2775, $R_{eff} = 3.26 \text{ kpc}$; NGC 0779, $R_{eff} = 2.35 \ kpc$) exhibit the most extreme LDMD values ($\rho_{DM,\odot} = 1.770$ and 1.230, respectively). This trend is directly linked to the halo concentration parameter, where systems with higher concentrations are more DMdominated, which consequently results in a higher inferred density at the equivalent Solar neighborhood radius.

While these compact systems are included in the full analysis, we exclude them for the purpose of estimating the final LDMD range, avoiding potential bias from these outliers. Our resulting LDMD estimate $0.17-0.46~GeV~cm^{-3}$ is therefore based on four galaxies from this work (NGC 7479, NGC 7606, NGC 5678, NGC 5878), five from de Isídio et al. (2024) (NGC 2903, NGC 3521, NGC 4579, NGC 4698, NGC 5055), and 127 TNG50 systems. This constrained range is consistent with most previous estimates for the MW and its analogs (see references in Table 3)

5.2. Galaxy-Halo connection

The intrinsic shape of a DM halo is a topic explored by many authors (Warren et al. 1992; Governato et al. 2012; Palau & Miralda-Escudé 2023). Seminal works based on DM-only simulations typically found prolate halos (Frenk et al. 1988), while later simulations that incorporated baryonic physics such as gas cooling (Dubinski 1994), star formation (Bryan et al. 2013; Di Cintio et al. 2013), AGN and stellar feedback (Grand et al. 2017; Nelson et al. 2019b) often produced more oblate, flattened distributions. The precise dynamical mecha-

Table 3. Comparison of LDMD estimates in the literature. The last column indicates the technique used to derive the LDMD estimates. Method abbreviations: Theo = theoretical; CE = centrifugal equilibrium; GM = global modeling; ML = microlensing; VM = vertical motion; SIM = simulations; PT = Pulsar timing measurements; SS = stellar streams. The asterisk symbol denotes estimates derived from MW analog sample analysis. A useful conversion is 1 M_{\odot} pc⁻³ = 37.96 GeV cm⁻³.

	LDMD	
Authors	${ m GeV~cm^{-3}}$	Method
Standard Halo Model	0.30	Theo
Catena & Ullio (2010)	0.39 ± 0.02	GM
Salucci et al. (2010)	0.43 ± 0.11	CE
Weber & de Boer (2010)	0.20 - 0.40	GM
Iocco et al. (2011)	0.20 - 0.56	$\mathrm{ML}\ \&\ \mathrm{GM}$
Bovy & Tremaine (2012)	0.30 ± 0.10	VM
Zhang et al. (2013)	0.25 ± 0.09	VM
Nesti & Salucci (2013)	0.47 ± 0.05	GM
Bienaymé, O. et al. (2014)	0.54 ± 0.04	VM
Sofue (2015)	0.26 ± 0.11	GM
Pato et al. (2015)	0.42 ± 0.02	GM
Huang et al. (2016)	0.32 ± 0.02	GM
McMillan (2017)	0.40 ± 0.04	GM & SIM
Eilers et al. (2019)	0.30 ± 0.03	GM
Karukes et al. (2020)	0.45 - 0.49	GM
Chakrabarti et al. (2021)	0.13 ± 1.32	PT
Palau & Miralda-Escudé (2023)	0.23 ± 0.02	${\rm SS}\ \&\ {\rm GM}$
Pillepich et al. (2024)	0.20 - 0.50	SIM*
de Isídio et al. (2024)	0.21 - 0.55	GM^*
This work	0.17 - 0.46	GM* & SIM*

nisms responsible for this transformation, and the extent to which baryons can alter the inner density profile of a halo, are not yet fully understood. Nevertheless, it is evident that there exists a strong connection between the luminous component and the DM halo structure (Wechsler & Tinker 2018).

Given the complex nature of galaxy formation, an effective way to address the galaxy-halo connection is to analyze scaling relations that link both components, that is, the stellar and halo masses. The abundance matching technique presented in Moster et al. (2010) – see Wechsler & Tinker 2018 for a recent review – yields a stellar-to-halo-mass relatin (SHMR) characterized by a steep power-law slope at low masses, which gradually flattens near a characteristic halo mass of $M_{200} \sim 10^{12} M_{\odot}$ and stellar mass $M_{\star} \sim 5 \times 10^{10} M_{\odot} (f_{\star} \sim 20\%)$. The physical interpretation of this transition and the precise location of different galaxy types (e.g., dwarfs,

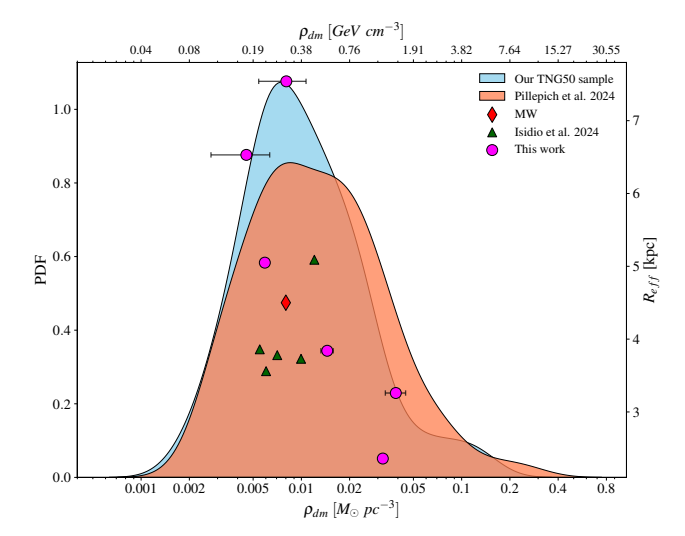


Figure 7. Comparison of the LDMD derived for our sample of 127 simulated MW analog galaxies (in sky blue) with values from the 130 TNG50 analogs studied in Pillepich et al. (2024) (coral), under a different selection criteria. In both samples we apply the equivalent Solar neighborhood definition detailed in Section 5.1. We include LDMD estimates for our observed galaxies (pink data points), the sample from de Isídio et al. (2024) (dark green triangles), and the estimate for the MW predicted by the Standard Halo Model ($\rho_{DM}=0.3~GeV~cm^{-3}$; red diamond), positioned according to their effective radius $R_{\rm eff}$.

spirals, ellipticals) within this framework remain subjects of active debate in the literature. Recent works using spatial and spectral high-resolution data also derive such trend (Posti, Lorenzo et al. 2019a,b; Posti & Fall 2021; Mancera Piña et al. 2022; Di Teodoro et al. 2022), following previous predictions in the literature (e.g., Moster et al. 2010, 2012; Rodríguez-Puebla et al. 2015). In this context, the star formation efficiency (f_{\star}) and the baryon fraction ($f_{\rm b}$) within our sample provide crucial insights into the remaining gas reservoir (the fuel available for future star formation) and offer valuable constraints on the fraction of "missing baryons" on galactic scales.

In Figure 8, we present the derived stellar mass (M_*) as a function of halo mass (M_{200}) for both the observational and the simulated TNG50 sample. For context, we include the SHMR from Moster et al. (2010) and the linear fit (in log-log space) using Posti & Helmi (2019) mass estimates from 110 disc galaxies in the SPARC database (Lelli et al. 2016). Our entire observed sample and the majority (> 50%) of TNG50 galaxies are concentrated above the $\approx 12 \log(M_{200}/M_{\odot})$ peak from Moster et al. (2010) relation, and below the cosmological baryonic mass limit ($f_{baryon}M_{200} = 0.188$, Aghanim et al. 2020). The data points from Mancera Piña et al.

(2022), exhibit significantly greater scatter than ours. This is a direct result of their sample composition, which includes both massive spirals and dwarf galaxies (22 and 10, respectively). Dwarf galaxies are typically DM-dominated (e.g., Oman et al. 2015) and consequently occupy the lower stellar mass region ($\log(M_*/M_\odot) \lesssim 9$) of the parameter space; this accounts for the broader distribution of datapoints from Mancera Piña et al. (2022). As we focus this work on MW analogs, which are more massive late-type galaxies, this dwarf galaxy locus is not covered by our sample. Galaxies from VIVA (Chung et al. 2009) and THINGS (Walter et al. 2008) surveys studied in de Isídio et al. (2024), are in strong agreement with our results.

We also show the stellar mass fraction normalized by the average cosmological baryon fraction in Figure 8. The y-axis, $f_{\star} \equiv M_{\star}/(f_{baryon}M_{200})$, represents the efficiency with which baryons have been converted into stars. Galaxies with higher f_{\star} values are those that are more stellar dominated. Half of our observational sample (NGC 7606, NGC 2775, NGC 0779) lies within the 1σ scatter of the Moster et al. (2010) relation, consistent with the expected peak in galaxy formation efficiency (Silk & Mamon 2012). The other half (NGC 7479, NGC 5678, NGC 5878) lies systematically above this relation. This suggests that these systems have, in fact, higher stellar mass fractions than predicted by Moster et al. 2013. The more massive halos in this subgroup appear to align with the relation by Posti & Fall (2021), where late-type galaxies may follow a monotonically rising SHMR, distinct from the declining trend seen in early-type systems. The isolated position of NGC 5878, a less massive spiral, in Figure 8 may indicate a distinct evolutionary pathway characterized by exceptionally high star formation efficiency.

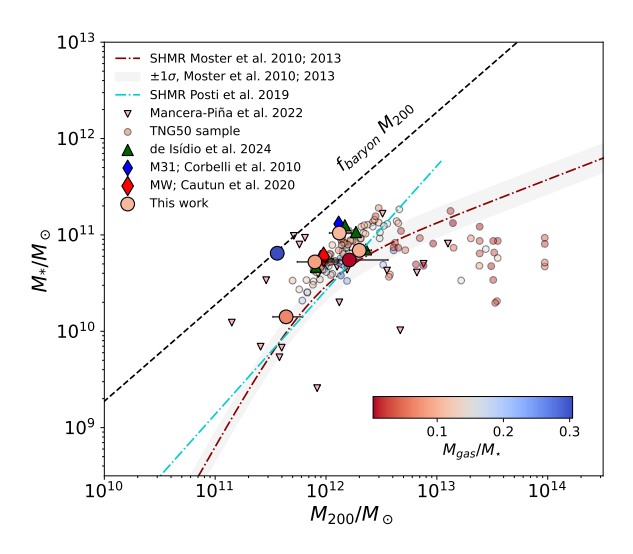
While our sample has a lower mass limit that could potentially bias a full analysis of the SHMR shape, the region of primary interest, $M_{\rm halo} \sim 10^{12} M_{\odot}$, is wellrepresented. The physical mechanisms responsible for the declining star formation efficiency at both the lowand high-mass ends of the SHMR are primarily linked to feedback processes. At the low-mass end, energetic feedback from young stars can effectively disrupt the interstellar medium and outweigh star formation (Veilleux et al. 2005, and references therein). At the high-mass end, feedback from active galactic nuclei (AGN) plays a critical role in driving powerful outflows (e.g., Weinberger et al. 2016; Harrison 2017). In both regimes, these feedback processes suppress the inflow and delay or prevent gas cooling, thereby promoting galactic quenching (Posti & Fall 2021). A reliable estimate of the gas mass (even as a lower limit, given the inherent loss of large-scale, diffuse emission in interferometric data) provides crucial insight into a galaxy's fuel reservoir and its star formation history. We analyze the gas-to-stellar mass ratio $(M_{\rm gas}/M_{\star})$, represented by the color scale in Figure 8. Despite the modest size of our observed sample, we identify a clear bimodality: gas-rich (blue) galaxies with $M_{\rm gas}/M_{\star} \gtrsim 10\%$, and gas-poor (red) galaxies with $M_{\rm gas}/M_{\star} \lesssim 5\%$ residing in DM halos of different masses. Figure 8 clearly shows a DM halo mass trend spanning from the most gas-rich to the less gas-rich system in our sample. This trend is consistent with the findings of Cui et al. (2021), who showed that at a fixed stellar mass, bluer galaxies tend to reside in less massive halos, while redder galaxies inhabit more massive ones. Conversely, at a fixed halo mass, bluer galaxies tend to have formed stars more efficiently, resulting in higher stellar masses, whereas redder galaxies typically exhibit lower stellar masses for the same halo mass. A complete explanation for the scatter in the SHMR requires detailed knowledge of individual halo assembly histories (e.g., Artale, María Celeste et al. 2019; Cui et al. 2021), which is beyond the scope of this work.

6. CONCLUSIONS

In this work we study a combined sample of 11 observed and 127 simulated MW analog galaxies to understand how DM is distributed in these systems. For the observational sample, we apply a full dynamical treatment to decompose the mass components within their halos; we use the 3D BAROLO algorithm to derive RCs by combining HI kinematics with mid-infrared imaging. This approach allows us to robustly account for the gravitational contributions of stars and gas, thereby isolating the DM component. Through a careful decomposition of these main galactic components, we show our derived RCs and the best-fit NFW values for concentration and M200 to model these galaxies' DM halos. The TNG50 simulated sample provides a diverse and statistically significant suite of analogs that allows us to compare stateof-the-art theoretical and empirical prescriptions with real data.

Our main results are summarized below.

(i) The NFW profile reproduces the HI-derived RCs of all observed MW-analog galaxies in our sample. Although the TNG50 DM density profiles show larger object-to-object scatter — reflecting the broader diversity of halo properties in a cosmological volume — their shapes remain consistent with NFW. This agreement across both data and simulations supports a working universality in the halo structure of MW analogs at galactic radii.



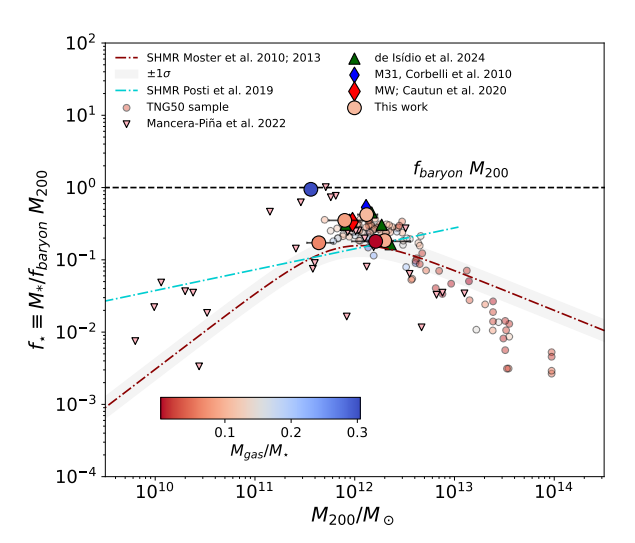


Figure 8. Top panel: Stellar-to-halo mass relation, SHMR. Bottom panel: Star formation efficiency, $f_{\star} \equiv M_{\star}/f_{baryon}M_{200}$. The dash-dotted dark red curve shows the SHMR from Moster et al. (2010), with its 1σ scatter. The teal line represents the linear SHMR we derived from a SPARC sample (Lelli et al. 2016) analyzed in (Posti & Helmi 2019). Light pink points correspond to data from Mancera Piña et al. (2022), while green triangles denote galaxies from the VIVA (Chung et al. 2009) and THINGS (Walter et al. 2008) surveys studied in de Isídio et al. (2024). The dashed black line indicates the universal baryon fraction ($f_{\rm b} = \Omega_{\rm b}/\Omega_{\rm m}$), representing the theoretical upper limit for the baryonic mass within a halo.

(ii) The inferred LDMD for our MW–analog sample falls in the range $0.17-0.46~GeV~cm^{-3}~(\approx 0.004-0.012~M_{\odot}~pc^{-3})$, consistent with MW values from the literature. The narrowness and MW consistency of this window—even for the most

- DM–dominated, compact halos—further points to an underlying universality in the inner halo of MW–like systems.
- (iii) Based on our derived DM, stellar and gas mass estimates (M₂₀₀, M_⋆, M_{gas}) for the combined sample of 138 MW analogs, we examine the stellar–to–halo mass relation (SHMR) and find a clear bimodality: at fixed M_⋆, gas–rich (blue) galaxies reside in less massive halos than gas–poor (red) systems; at fixed M₂₀₀, blue galaxies have higher M_⋆ than red ones. This indicates substantial diversity in baryonic growth histories even among halos of comparable mass.

This work demonstrates the potential of analyzing HI kinematics in nearby galaxies to overcome the challenges of studying the DM halo of the MW from within. Next generation radio telescopes, such as the ngVLA and SKA, will enable detailed kinematic studies of cold gas disks in thousands of galaxies, both nearby and at high redshift. Their unprecedented sensitivity and resolution will provide a deeper understanding of the connection between galaxies and their halos. This refined view of DM distribution on galactic scales will, in turn, deliver

crucial astrophysical context for interpreting the results of upcoming direct detection experiments on Earth.

ACKNOWLEDGMENTS

M.C.C.S. acknowledges the support of the Brazilian National Research Council (CNPq, Brazil). K.M.D. acknowledges the support of the Serrapilheira Institute (grant Serra-1709-17357) as well as that of the Brazilian National Research Council (CNPq grant 308584/2022-8) and of the Rio de Janeiro State Research Foundation (FAPERJ grant E-26/200.952/2022), Brazil. T.S.G. would also like to thank the support of CNPq (Productivity in Research grant 314747/2020-6) and the FAPERJ (Young Scientist of Our State grant E-26/201.309/2021). DCR thanks Centro Brasileiro de Pesquisas Físicas (CBPF) for hospitality, where part of this work was done. He also acknowledges CNPq, Fundação de Amparo à Pesquisa e Inovação do Espírito Santo (FAPES, Brazil) and Fundação de Apoio ao Desenvolvimento da Computação Científica (FACC, Brazil) for partial support.

REFERENCES

Aalbers J., et al., 2023, Physical Review Letters, 131 Aghanim N., et al., 2020, Astronomy & Earphysics, 641, A6

Akerib D. S., et al., 2020, Phys. Rev. D, 101, 052002 Aprile E., et al., 2017, Phys. Rev. Lett., 119, 181301

Artale, María Celeste Pedrosa, Susana E. Tissera, Patricia B. Cataldi, Pedro Di Cintio, Arianna 2019, A&A, 622, A197

Bienaymé, O. et al., 2014, A&A, 571, A92

Biswas P., Kalinova V., Roy N., Patra N. N., Tyulneva N., 2023, Monthly Notices of the Royal Astronomical Society, 524, 6213–6228

Bosma A., 1978, PhD thesis, University of Groningen, Netherlands

Bosma A., 1981, AJ, 86, 1825

Bovy J., Tremaine S., 2012, ApJ, 756, 89

Bryan S. E., Kay S. T., Duffy A. R., Schaye J., Dalla Vecchia C., Booth C. M., 2013, MNRAS, 429, 3316

CASA Team et al., 2022, PASP, 134, 114501

Carignan C., Chemin L., Huchtmeier W. K., Lockman F. J., 2006, The Astrophysical Journal, 641, L109–L112

Catena R., Ullio P., 2010, Journal of Cosmology and Astroparticle Physics, 2010, 004–004

Catinella B., et al., 2010, MNRAS, 403, 683

Chakrabarti S., et al., 2020, The Astrophysical Journal Letters, 902, L28

Chakrabarti S., Chang P., Lam M. T., Vigeland S. J., Quillen A. C., 2021, The Astrophysical Journal Letters, 907, L26

Chakrabarti S., Stevens D. J., Wright J., Rafikov R. R., Chang P., Beatty T., Huber D., 2022, ApJL, 928, L17

Chowdhury A., Kanekar N., Chengalur J. N., 2022, The Astrophysical Journal Letters, 935, L5

Chung A., van Gorkom J. H., Kenney J. D. P., Crowl H., Vollmer B., 2009, AJ, 138, 1741

Collaboration T. L., et al., 2015, LUX-ZEPLIN (LZ) Conceptual Design Report (arXiv:1509.02910)

Cui W., Davé R., Peacock J., Anglés-Alcázar D., Yang X., 2021, Nature Astronomy, 5, 1069

Davis M., Efstathiou G., Frenk C. S., White S. D. M., 1985, ApJ, 292, 371

Di Cintio A., Brook C. B., Macciò A. V., Stinson G. S., Knebe A., Dutton A. A., Wadsley J., 2013, Monthly Notices of the Royal Astronomical Society, 437, 415–423

Di Teodoro E. M., et al., 2022, Monthly Notices of the Royal Astronomical Society, 518, 6340

Dubinski J., 1994, ApJ, 431, 617

- Dutton A. A., Macciò A. V., 2014, Monthly Notices of the Royal Astronomical Society, 441, 3359–3374
- Eilers A.-C., Hogg D. W., Rix H.-W., Ness M. K., 2019, The Astrophysical Journal, 871, 120
- Elia D., et al., 2022, The Astrophysical Journal, 941, 162
- Foreman-Mackey D., Hogg D. W., Lang D., Goodman J., 2013, PASP, 125, 306
- Frenk C. S., White S. D. M., Davis M., Efstathiou G., 1988, ApJ, 327, 507
- Governato F., et al., 2012, Monthly Notices of the Royal Astronomical Society, 422, 1231–1240
- Grand R. J. J., et al., 2017, MNRAS, 467, 179
- Harrison C. M., 2017, Nature Astronomy, 1, 0165
- Hou L. G., Han J. L., 2014, Astronomy & Samp; Astrophysics, 569, A125
- Huang Y., et al., 2016, MNRAS, 463, 2623
- Iocco F., Pato M., Bertone G., Jetzer P., 2011, JCAP, 2011, 029
- Iocco F., Pato M., Bertone G., 2015, Nature Physics, 11, 245
- Kamphuis P., Józsa G. I. G., Oh S.-H., Spekkens K., Urbancic N., Serra P., Koribalski B. S., Dettmar R.-J., 2015, Monthly Notices of the Royal Astronomical Society, 452, 3139
- Kapteyn J. C., 1922, ApJ, 55, 302
- Karukes E., Benito M., Iocco F., Trotta R., Geringer-Sameth A., 2020, Journal of Cosmology and Astroparticle Physics, 2020, 033–033
- Lelli F., McGaugh S. S., Schombert J. M., 2016, The Astronomical Journal, 152, 157
- Licquia T. C., Newman J. A., 2015, ApJ, 806, 96
- Mancera Piña P. E., Fraternali F., Oosterloo T., Adams E. A. K., di Teodoro E., Bacchini C., Iorio G., 2022, MNRAS, 514, 3329
- McMillan P. J., 2017, MNRAS, 465, 76
- Moster B. P., Somerville R. S., Maulbetsch C., van den Bosch F. C., Macciò A. V., Naab T., Oser L., 2010, The Astrophysical Journal, 710, 903–923
- Moster B. P., Naab T., White S. D. M., 2012, Monthly Notices of the Royal Astronomical Society, 428, 3121–3138
- Moster B. P., Naab T., White S. D. M., 2013, MNRAS, 428, 3121
- Munoz-Mateos J. C., et al., 2015, The Spitzer Survey of Stellar Structure in Galaxies (S4G): Stellar Masses, Sizes and Radial Profiles for 2352 Nearby Galaxies (arXiv:1505.03534), https://arxiv.org/abs/1505.03534
- Muñoz-Mateos J. C., et al., 2013, The Astrophysical Journal, 771, 59

- Navarro J. F., Frenk C. S., White S. D. M., 1996, ApJ, 462, 563
- Nelson D., et al., 2019a, Computational Astrophysics and Cosmology, 6, 2
- Nelson D., et al., 2019b, Monthly Notices of the Royal Astronomical Society, 490, 3234–3261
- Nesti F., Salucci P., 2013, Journal of Cosmology and Astroparticle Physics, 2013, 016–016
- Oman K. A., et al., 2015, Monthly Notices of the Royal Astronomical Society, 452, 3650–3665
- Oort J. H., 1932, BAN, 6, 249
- Palau C. G., Miralda-Escudé J., 2023, Monthly Notices of the Royal Astronomical Society, 524, 2124–2147
- Pato M., Iocco F., 2015, The Astrophysical Journal, 803, L3
- Pato M., Iocco F., Bertone G., 2015, Journal of Cosmology and Astroparticle Physics, 2015, 001–001
- Peebles P. J. E., 1982, ApJL, 263, L1
- Pillepich A., et al., 2018, MNRAS, 473, 4077
- Pillepich A., et al., 2019, Monthly Notices of the Royal Astronomical Society, 490, 3196–3233
- Pillepich A., et al., 2024, MNRAS, 535, 1721
- Posti L., Fall S. M., 2021, Astronomy & Samp; Astrophysics, 649, A119
- Posti L., Helmi A., 2019, Astronomy & Emp; Astrophysics, 621, A56
- Posti, Lorenzo Fraternali, Filippo Marasco, Antonino 2019a, A&A, 626, A56
- Posti, Lorenzo Marasco, Antonino Fraternali, Filippo Famaey, Benoit 2019b, A&A, 629, A59
- Querejeta M., et al., 2015, ApJS, 219, 5
- Reid M. J., Dame T. M., 2016, ApJ, 832, 159
- Reid M. J., et al., 2014, ApJ, 783, 130
- Riess A. G., et al., 1998, AJ, 116, 1009
- Rodríguez-Puebla A., Avila-Reese V., Yang X., Foucaud S., Drory N., Jing Y. P., 2015, ApJ, 799, 130
- Rogstad D. H., Lockhart I. A., Wright M. C. H., 1974, ApJ, 193, 309
- Rubin V. C., Ford Jr. W. K., Thonnard N., 1980, ApJ, 238, 471
- Saintonge A., Catinella B., 2022, Annual Review of Astronomy and Astrophysics, 60, 319–361
- Salucci P., Lapi A., Tonini C., Gentile G., Yegorova I., Klein U., 2007, Monthly Notices of the Royal Astronomical Society, 378, 41–47
- Salucci P., Nesti F., Gentile G., Frigerio Martins C., 2010, Astronomy & Astrophysics, 523, A83
- Sheth K., et al., 2010, PASP, 122, 1397

- Silk J., Mamon G. A., 2012, The Current Status of Galaxy Formation (arXiv:1207.3080),
 - doi:https://doi.org/10.1088/1674-4527/12/8/004, https://arxiv.org/abs/1207.3080
- Silverwood H., Easther R., 2019, Publ. Astron. Soc. Austral., 36, e038
- Sofue Y., 2013, PASJ, 65, 118
- Sofue Y., 2015, PASJ, 67, 75
- Sofue Y., Rubin V., 2001, ARA&A, 39, 137
- Spergel D. N., et al., 2007, ApJS, 170, 377
- Steigman G., Turner M. S., 1985, Nuclear Physics B, 253, $375\,$
- Teodoro E. M. D., Fraternali F., 2015, Monthly Notices of the Royal Astronomical Society, 451, 3021
- Tremaine S., Gunn J. E., 1979, PhRvL, 42, 407
- Undagoitia T. M., Rauch L., 2015, Journal of Physics G: Nuclear and Particle Physics, 43, 013001
- Veilleux S., Cecil G., Bland-Hawthorn J., 2005, ARA&A, 43, 769

- Walter F., Brinks E., de Blok W. J. G., Bigiel F., Kennicutt Jr. R. C., Thornley M. D., Leroy A., 2008, AJ, 136, 2563
 Warren M. S., Quinn P. J., Salmon J. K., Zurek W. H., 1992, ApJ, 399, 405
- Watkins, A. E. et al., 2022, A&A, 660, A69
- Weber M., de Boer W., 2010, Astronomy and Astrophysics, 509, A25
- Wechsler R. H., Tinker J. L., 2018, ARA&A, 56, 435Weinberger R., et al., 2016, Monthly Notices of the Royal Astronomical Society, 465, 3291–3308
- White S. D. M., Frenk C. S., Davis M., 1983, ApJL, 274, L1
 Zhang L., Rix H.-W., van de Ven G., Bovy J., Liu C., Zhao G., 2013, ApJ, 772, 108
- Zhou S., Aragón-Salamanca A., Merrifield M., Andrews B. H., Drory N., Lane R. R., 2023, Monthly Notices of the Royal Astronomical Society, 521, 5810–5825
- de Isídio N. G., et al., 2024, The Astrophysical Journal, 971, 69